Origin of chemical contrast in low-energy electron reflectivity of correlated multivalent oxides: The case of ceria

Jan Ingo Flege,* Björn Kaemena, Axel Meyer, and Jens Falta
Institute of Solid State Physics, University of Bremen, Otto-Hahn-Allee 1, 28359 Bremen, Germany

Sanjaya D. Senanayake
Chemistry Department, Brookhaven National Laboratory, Upton, New York 11973, USA

Jerzy T. Sadowski
Center for Functional Nanomaterials, Brookhaven National Laboratory, Upton, New York 11973, USA

R. D. Eithiraj
Donostia International Physics Center (DIPC), Paseo Manuel de Lardizabal 4, 20018 San Sebastián/Donostia, Basque Country, Spain

Eugene E. Krasovskii
Departamento de Física de Materiales, Facultad de Ciencias Químicas, Universidad del Pais Vasco/Euskal Herriko Unibertsitatea, Apartado 1072, 20080 San Sebastián/Donostia, Basque Country, Spain;
Donostia International Physics Center (DIPC), Paseo Manuel de Lardizabal 4, 20018 San Sebastián/Donostia, Basque Country, Spain; and IKERBASQUE, Basque Foundation for Science, 48011 Bilbao, Spain

(Received 3 September 2012; revised manuscript received 19 November 2013; published 23 December 2013)

A combined experimental and theoretical study of the local chemistry of cerium oxide films and islands on Ru(0001) is presented. Based on intensity-voltage low-energy electron microscopy [$I(V)$-LEEM] and resonant x-ray photoemission spectroscopy, we establish a one-to-one correspondence between the local oxidation state of Ce^{3+} [cubic $Ce_2O_3(111)$] and Ce^{4+} [cubic $CeO_2(111)$] and their respective spatially resolved $I(V)$ curves. *Ab initio* scattering theory explains the difference between the $I(V)$ curves in the low-energy range in terms of the $k_{\parallel} = 0$ projected band structure arising from the different structure of the Ce *5d* states in fully oxidized and reduced ceria. The theoretical analysis unambiguously attributes the LEEM contrast observed for chemically reduced cerium oxide to a variation in oxidation state on the nanometer scale, which is not present for the as-grown islands.

DOI: 10.1103/PhysRevB.88.235428 PACS number(s): 68.37.Nq, 68.55.A−, 71.15.−m, 73.20.−r

I. INTRODUCTION

Cerium oxide is a remarkably versatile material and has attracted persistent interest due to its wide range of existing and potential applications in, e.g., catalysis,[1,2] energy harvesting and storage,[3,4] sensing,[5–7] and microelectronics.[8] Its inherent structural and electronic variability arises from the unfilled shell of highly localized *4f* electrons in the valence band region, making it a particularly attractive model system in fundamental studies of electron correlation and chemical bonding in binary metal oxides. Depending on its formal oxidation state, i.e., Ce^{3+} or Ce^{4+}, three major crystallographic phases have been identified: a hexagonal structure for the sesquioxide Ce_2O_3 (space group $P\bar{3}2/m1$, No. 164), a $CeO_{1.5+\delta}$ bixbyite phase ($Ia\bar{3}$, No. 206) for slightly higher oxygen concentration ($\delta \ll 0.5$), and a fluorite phase ($Fm\bar{3}m$, No. 225) for cerium dioxide, CeO_2.[1] The facile transformation especially between the bixbyite and the fluorite phase is the main reason for the pronounced oxygen storage capacity of ceria, i.e., its ability to take up and release oxygen under oxidizing and reducing conditions, respectively. This effective switching between oxidation states makes it a crucial component in, e.g., catalytic converters of today's automotive industry[9,10] as well as future-generation intermediate-temperature solid oxide fuel cells.[11] For optimized device performance a thorough understanding of the structure-function relationship of nanostructured ceria-based compounds is essential.

Many efforts have been undertaken to unravel the structural and electronic properties of the different crystalline cerium oxide phases in bulk form[1] or as thin epitaxial films.[12] So far, the main focus has been on structure determination and on the occupied electronic structure. In particular, several attempts were made in characterizing the local thermal reduction of CeO_2 in real space on the atomic scale using scanning tunneling microscopy[13] and atomic force microscopy.[14] While these techniques provide valuable insight into the formation of atomic-scale "Ce^{3+}" defects, they usually do not offer sufficient temporal or spatial resolution due to lack of thermal stability to allow *in situ* probing of chemical transformations at reaction conditions. In this respect, synchrotron-based x-ray photoemission electron microscopy and related approaches also are very promising since they transfer established concepts for oxidation state analysis to the nanoscale.[15] Yet, it would be attractive to complement these studies by methods that offer an even enhanced spatial and temporal resolution.

Here we elucidate the origin of the chemical contrast in the specular reflectivity of low-energy electrons from a prototypical multivalent, correlated electron system, i.e., cerium oxide (CeO_x, $1.5 \leqslant x \leqslant 2$). To this end, we have prepared cerium oxide surfaces of varying stoichiometry, which were

investigated *in situ* using a combination of laterally averaging resonant photoemission spectroscopy (RPES) as well as nanoscopic, very-low-energy electron diffraction (VLEED). These experiments were performed inside a spectroscopic photoemission low-energy electron microscope (SPE-LEEM). Applying *ab initio* scattering theory, we demonstrate that the most important differences for fully oxidized and reduced ceria in the $\mathbf{k}_{\parallel} = 0$ projected band structure, which determines the electron reflectivity,[16–22] are due to the localized Ce *5d* states. The transmission by these highly localized Ce *5d* states is shown to dominate the energy-dependent sample reflectivity $R(E)$. Owing to their atomiclike character, the Ce *5d*-derived bands are strongly modified by the variation in Ce *4f* occupation and, thus, are sensitive to the change in oxidation state. Since these $R(E)$ spectra are a local representation of the electronic structure on the very-few-nanometer scale, they provide a nanometric probe of the oxidation state. In the following, this capability is demonstrated by *in situ* LEEM on nearly perfect and defective cerium oxide nanoislands grown on Ru(0001), which is a frequently studied inverse model catalyst, e.g., for the water-gas-shift reaction.[23]

II. EXPERIMENTAL

The LEEM and RPES measurements were performed in a commercial Elmitec SPE-LEEM (spectroscopic photoemission and low-energy electron microscope) installed at beamline U5UA of the National Synchrotron Light Source (NSLS) at Brookhaven National Laboratory (BNL), Upton, NY (USA). This setup enables *in situ* microscopy with either low-energy electrons or monochromatized photons from the storage ring and also spatially resolved photoemission spectroscopy with synchrotron radiation.[24] Atomic force microscopy (AFM) was conducted *ex situ* at the Center for Functional Nanomaterials (CFN) also located at BNL using a commercial system (Veeco Multimode V). Data processing and analysis were performed using the software package GXSM.[25]

Polished Ru(0001) single crystals (Mateck) with a nominal orientation better than 0.1° served as substrates and were cleaned by repeated cycles of oxygen dosing followed by high-temperature flash annealing as described in Ref. 26. Cerium oxide growth was achieved by reactive molecular beam epitaxy under ultrahigh-vacuum (UHV) conditions, with metallic Ce deposited from a home-built, calibrated electron beam evaporator at substrate temperatures between 360 °C and 800 °C and preset oxygen (O_2) background pressures between 1×10^{-8} and 5×10^{-7} mbar.

III. RESULTS AND DISCUSSION

A. Cerium oxide growth and island morphology

On ruthenium, cerium oxide adopts a Volmer-Weber growth mode, as can be seen from the time-lapse LEEM image sequence in Figs. 1(a)–1(e) recorded for deposition of metallic cerium in an oxygen background pressure of $p = 5 \times 10^{-7}$ Torr and at a substrate temperature of 800 °C. Stable nuclei are most frequently observed at atomic step edges and step bunches, which are represented as dark bands. Further deposition leads to the formation of essentially triangular, single-crystalline islands, whose apices exhibit varying orientations relative to the substrate and whose average size and density depend on growth temperature.[27] From AFM [Fig. 1(f)], it is evident that the islands typically are only a few nm thin and overgrow the substrate atomic steps in a carpetlike fashion.

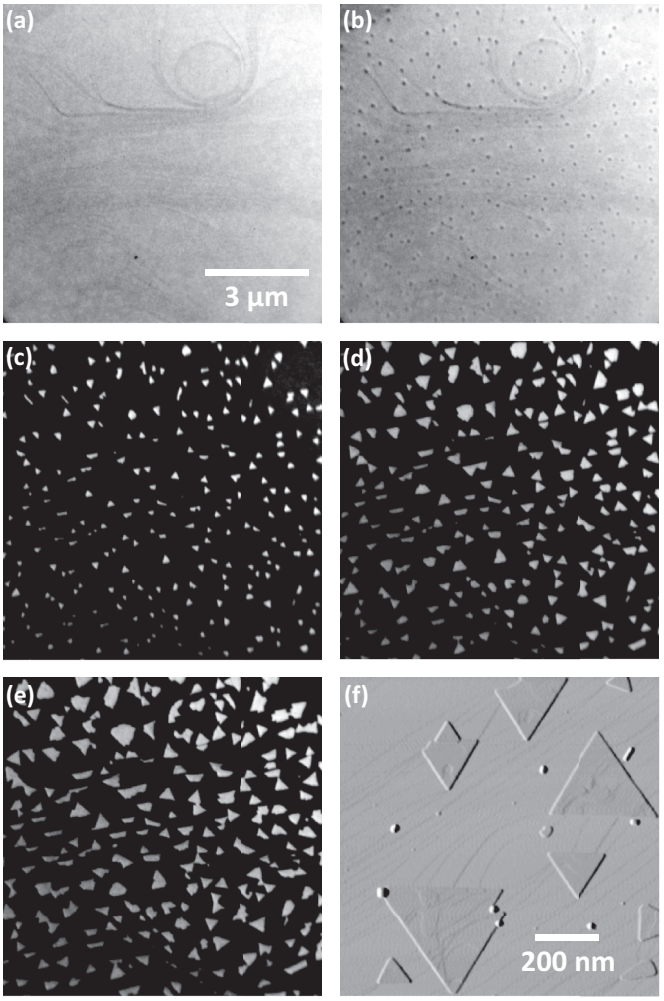

FIG. 1. (a)–(e) Low-energy electron micrographs illustrating the growth of cerium oxide on Ru(0001) by reactive molecular beam epitaxy at 800 °C and an O_2 partial pressure of 5×10^{-7} Torr. The change in contrast between (a),(b) and (c)–(e) is due to a change in electron energy. Coverages: (a) 0 ML, (b) 0.02 ML, (c) 0.20 ML, (d) 0.60 ML, and (e) 1.21 ML. (f) Close-up view of triangular, single-crystalline cerium oxide islands as imaged by *ex situ* AFM (image differentiated).

While micron-scale selected-area low-energy electron diffraction as well as x-ray photoemission confirm the growth of fluoritelike, (111)-oriented CeO_x islands,[27] chemical identification on the true nanoscale remains very challenging to achieve with these methods. This, however, is mandatory for *in situ* analysis of the local oxidation state under reaction conditions.

B. Linking oxidation state and intensity-voltage curves

The $I(V)$-LEEM approach has already demonstrated its capability of providing detailed local information on adsorbate

film thickness and layer spacings,[28] elemental composition of bimetallic surface alloys,[29] and identification of individual oxygen-rich phases in chemical reactions,[26,30] at length scales down to less than 10 nm. In the following, we demonstrate that $I(V)$-LEEM also allows accessing the local oxidation state of multivalent oxide compounds and that it additionally provides detailed information about the unoccupied band structure and electronic correlation effects.

To obtain quantitative information about the amount of Ce^{3+} and Ce^{4+} species, we prepared continuous ceria films in the SPE-LEEM system by extended deposition at reduced substrate temperature of 430 °C and an O_2 partial pressure of 1×10^{-8} mbar, in a similar vein to the original recipe by Mullins and co-workers.[31] These continuous films enable the use of laterally averaged RPES monitoring the Ce *4f*-related peaks in valence band spectra following resonant excitation of the Ce *4d* core level by monochromatized synchrotron radiation. This technique was first applied by the Matolin group to quantify the ceria oxidation state with very high sensitivity.[32,33] Briefly, depending on the photon energy and the resonance energy for the specific oxidation state, i.e., for Ce^{3+} (121.5 eV) or Ce^{4+} (124.5 eV), strongly enhanced photoemission is observed. Furthermore, if compared to the relative intensities in photoemission spectra taken in an off-resonance condition (115 eV) below the Ce *4d* level, it yields a precise measure of the relative abundance of Ce^{3+} and Ce^{4+} species in the probed region.[33] Here, we apply the same methodology in the SPE-LEEM setup to establish a one-to-one correspondence between the energy-dependent reflectivity, i.e., the $I(V)$ curve, and the corresponding oxidation state to sequentially enable local analysis using the full capabilities of $I(V)$-LEEM.

In Fig. 2, we present RPES data along with the corresponding $I(V)$ curves recorded for ceria films after various treatments. In the as-grown state [Fig. 2(a)], we observe a pronounced change of the peak intensities in the valence band spectra for both the Ce^{3+} and the Ce^{4+}

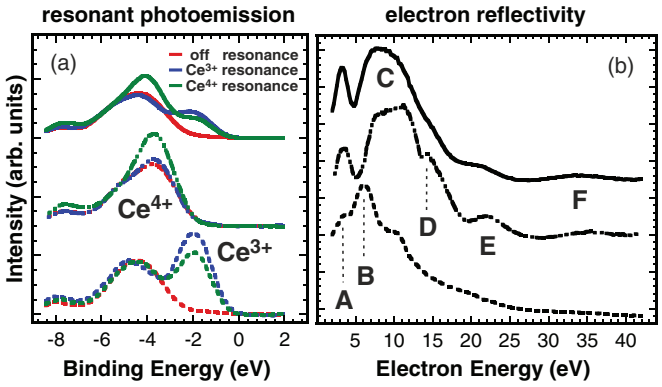

FIG. 2. (Color online) (a) RPES data of cerium oxide on Ru(0001): as grown at reduced O_2 pressure (solid curves), after postoxidation by O_2 (dash-dotted curves), and after reduction by methanol exposure (dashed curves). (b) Electron reflectivity data for cerium oxide on Ru(0001) acquired at elevated temperature corresponding to the RPES data presented in (a): as grown (top), after oxidation by O_2 (center), and after reduction by methanol exposure and subsequent annealing (bottom).

resonance energies. From the ratio $D(Ce^{3+})/D(Ce^{4+})$ of the individual resonance enhancements $D(Ce^{3+},Ce^{4+}) \equiv I_{res}(Ce^{3+},Ce^{4+}) - I_{off-res}(Ce^{3+},Ce^{4+})$ for both ionic species, an average stoichiometry of $CeO_{1.73}$ may be inferred[33] to within a few percent. The corresponding $I(V)$ curve, which is displayed in Fig. 2(b), shows two pronounced maxima in the very-low-energy range (labeled "A" and "C", respectively), a rather weak shoulder "E", and a broad maximum "F".

However, after postoxidation at 430 °C and an O_2 partial pressure of 2×10^{-6} Torr, both the RPES [Fig. 2(a)] and the $I(V)$ [Fig. 2(b)] data differ significantly from their as-grown counterparts. First, the presence of a fully oxidized CeO_2 film can readily be deduced from the complete absence of the Ce^{3+} resonance peak. Second, the $I(V)$ curve also exhibits systematic changes, the most prominent being the change of the shape of feature C, the appearance of a new shoulder "D", as well as the shape of feature E, which is discernible as a distinct peak at slightly increased electron energy. Also, a similar shift in energy can be observed for feature F.

Cyclic exposure to methanol at a partial pressure of 1×10^{-6} Torr followed by thermal annealing at 480 °C induces complete reduction of the cerium oxide film as evidenced by RPES depicted in Fig. 2(a). While there is no difference in the resonance and off-resonance Ce^{4+} peak intensity, the Ce^{3+}-related valence band peak is strongly developed, and is even more pronounced than for the as-grown sample. Hence, these data confirm an average stoichiometry of $CeO_{1.5}$ after reduction by methanol. This profound difference is again reflected by the $I(V)$ curve, which in this case exhibits a new maximum "B", a significantly reduced intensity of C, and the absence of shoulder D. Also, E apparently turns into a broad shoulder, while peak F has shifted toward lower electron energies.

C. *Ab initio* scattering calculations for cerium oxide

In the previous section, we have established that the $I(V)$ curves are characteristic of the stoichiometry of the cerium oxide crystal. $I(V)$ curve shapes in the VLEED region are closely related to the unoccupied band structure, which, especially in correlated electron systems, can be expected to substantially deviate from free-electron-like behavior. Thus, in interpreting $I(V)$ curves, it is important to fully take into account band structure effects. We have performed an analysis of the electron reflectivity $R(E)$ of $CeO_2(111)$ and both cubic $Ce_2O_3(111)$ and hexagonal $Ce_2O_3(0001)$ surfaces based on an *ab initio* scattering theory, in which both the bulk band structure and the potential at the surface are treated realistically. The relaxation of the surface layers[34] is neglected in the present work; i.e., the bulk geometry is assumed to hold right up to the surface. We expect surface relaxations to be less significant at very low energies, where the inelastic scattering is reduced, and the elastic scattering in the bulk is most important.

As the general computational methodology has been presented in detail in our preceding work on NiO,[35] here we only briefly recap the main steps and state the essential approximations. First, a self-consistent crystal potential in the local density approximation (LDA) is constructed[36] both for the bulk crystal and for the surface, the latter being obtained from a supercell made of a slab and a vacuum region. Thus,

the elastic scattering is treated fully *ab initio*, and the crystal structure is not being adjusted to the experimental spectrum.

Generally, elastic scattering determines the energy location of the maxima and minima of the $R(E)$ curve, but the intensity and sharpness of the structures is known to depend on inelastic scattering.[37] The latter is described by the optical potential, the energy-dependent imaginary potential V_i, which is spatially constant in the crystal and zero in the vacuum half space. The LEED wave functions are obtained as solutions of the Schrödinger equation for the complex potential using the augmented-plane-waves-based embedding method.[38] At present, it is not possible to determine the optical potential from first principles; however, its typical values and qualitative energy dependence $V_i(E)$ are known from experience, and they are not strongly material dependent.[39–43] To make the comparison of CeO_2 and Ce_2O_3 maximally conclusive we use the same linearly growing function $V_i(E)$ [Fig. 3(c)] and the same computational parameters for both crystals.

In contrast to the simple fluorite structure of CeO_2, the bixbyite structure of Ce_2O_3 has 16 formula units per unit cell, which is computationally forbidding. A much simpler crystal lattice for Ce_2O_3, which enables *ab initio* calculations but still closely mimics the bixbyite reference structure, can be derived from a 2×2 fluorite supercell with one oxygen vacancy per unit cell; see Ref. 44. Another difficulty with the reduced oxide arises from the partially occupied Ce *4f* shell, which cannot be obtained within a one-particle approach.

The *4f* electrons do not contribute to the LEED wave functions, as they lie below the vacuum level;[45] however, via the Coulomb interaction they affect the unoccupied scattering states. One way to force the actual occupancy of the *4f* shell is the LDA + U approach.[46–49] In the present work, we achieve this by including one *4f* electron per atom into the atomic core, so the *4f* band of Kohn-Sham eigenvalues remains unoccupied.

At energies of several eV above the vacuum level, the states carrying electron current are especially sensitive to the *4f* shell because the Ce *5d* states there retain their localized atomiclike character. Generally, the *5d* states form narrow bands with a small group velocity normal to the surface, and one would not expect them to transmit any significant fraction of the incident current into the crystal. Still, in CeO_2 the conducting bands have an appreciable contribution of *5d* character; see Figs. 3(a), 3(b), and 3(h). Figures 3(f)–3(h) compare the Ce *5d* band in the cubic and the hexagonal Ce_2O_3 crystals with the fluorite CeO_2.

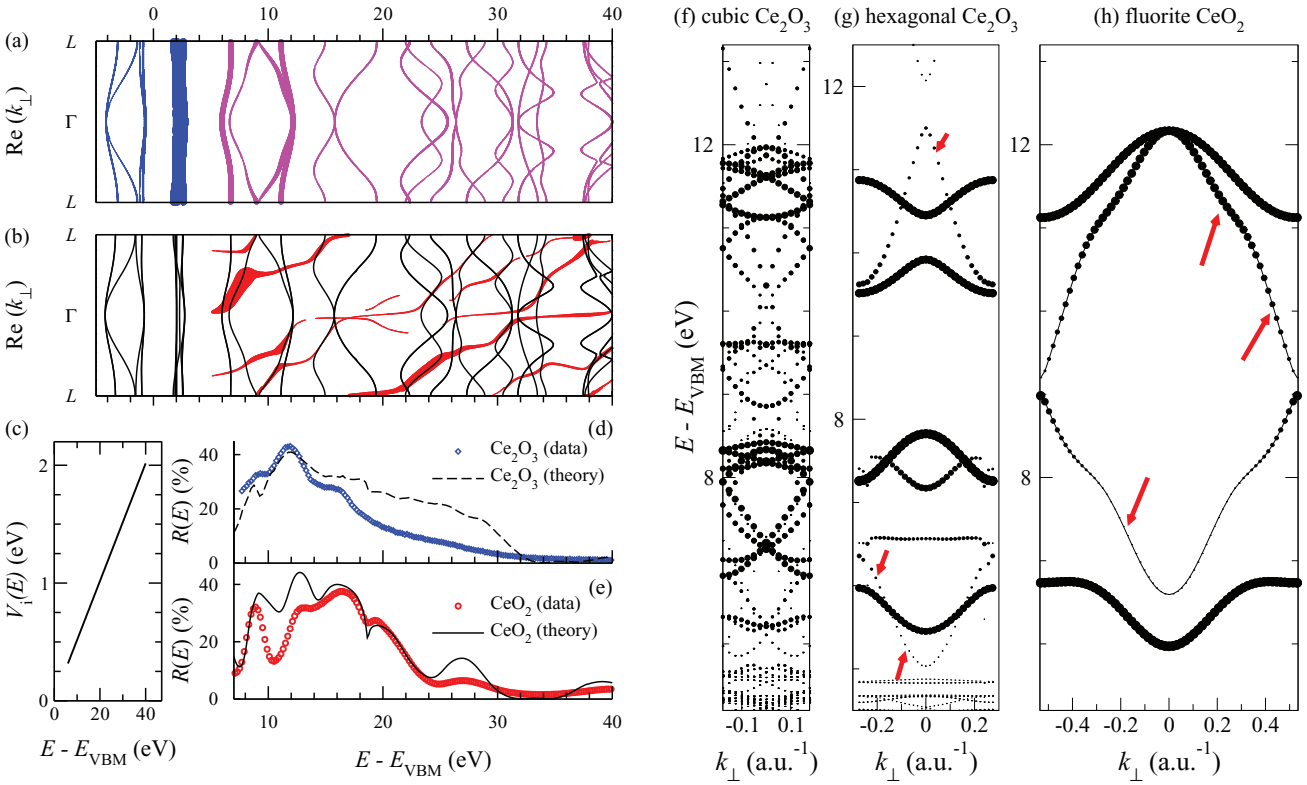

FIG. 3. (Color online) (a) $k_\parallel = 0$-projected band structure of $CeO_2(111)$ with thickness of the line indicating angular-momentum character of the bands (f character below 5 eV, d character above 5 eV); (b) $k_\parallel = 0$-projected band structure of $CeO_2(111)$ with thickness of the branch indicating the Bloch-wave resolved transmitted sample current; (c) assumed energy dependence of the optical potential $V_i(E)$; (d) experimental (open diamonds) and calculated (dashed line) electron reflectivity $R(E)$ for $Ce_2O_3(111)$; and (e) experimental (open circles) and calculated (solid line) electron reflectivity $R(E)$ for $CeO_2(111)$. The subfigures (a),(b),(d),(e) share the same abscissa. E_{VBM} denotes the valence band maximum. Also note that the "thick" line in (b) is not symmetric about the Γ point because only the waves that travel inside the crystal (i.e., have the same sign of the group velocity) enter the LEED state. (f)–(h) Comparison of the energy-momentum distribution of partial charges of d character in (111)-oriented cubic and (0001)-oriented hexagonal cerium oxide crystals for $k_\parallel = 0$. The size of the circle is proportional to the d-projected charge in the Ce sphere. For the fluorite CeO_2 (h) and for the hexagonal Ce_2O_3 (g) the conducting bands are indicated by red arrows. Panel (h) is a magnified fragment of panel (b). The energy axis for $Ce_2O_3(0001)$ has been shifted to align the Ce *5d* bands of all structures.

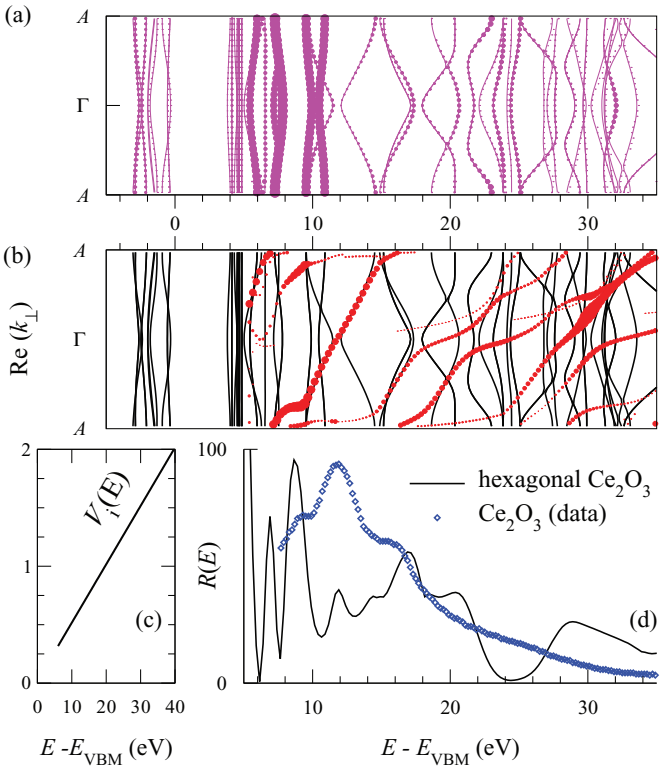

FIG. 4. (Color online) (a) $k_\parallel = 0$ projected band structure of hexagonal $Ce_2O_3(0001)$ with thickness of the line indicating the d character of the bands. (The f-character bands are at the bottom of the conduction band.) (b) $k_\parallel = 0$-projected band structure of $Ce_2O_3(0001)$: thin black lines show the real band structure, and the circles indicate the Bloch waves that effect the transmission of the incident current into the crystal. The size of the circle is proportional to the partial transmitted current. (c) Assumed energy dependence of the optical potential $V_i(E)$. (d) Calculated electron reflectivity $R(E)$ for the hexagonal $Ce_2O_3(0001)$ and acquired Ce_2O_3 $I(V)$ data.

In all the crystals the *5d* states occupy an interval of about 6 eV just above the *4f* band. For the fluorite CeO_2 and for the hexagonal Ce_2O_3 the conducting bands (i.e., the partial Bloch waves that transmit the incident current) are indicated by red arrows. They correspond to thick fragments of the red line in the conducting band structure plots of Fig. 3(b) for CeO_2 and Fig. 4(b) for hexagonal Ce_2O_3.

In both sesquioxides, the d contribution to the current carrying states at around $E - E_{VBM} = 10$–11 eV is much smaller than in CeO_2. This is in agreement with the data of Figs. 3(f)–3(h): The *5d* bands in both cubic and hexagonal Ce_2O_3 have considerably smaller group velocities than in CeO_2, which points to their more localized character. This is especially well seen for the hexagonal Ce_2O_3 [Fig. 3(g)], owing to its simple band structure and relatively large (compared to the cubic Ce_2O_3) Brillouin zone extent perpendicular to the surface. Figures 4(a) and 4(b) show that in the hexagonal Ce_2O_3 above 9 eV the current is carried by a highly dispersive band, which does not hybridize with the *5d* states.

Our theory yields convincing agreement with the experiment simultaneously for CeO_2 and for the cubic ("bixbyite") Ce_2O_3; see Figs. 3(d) and 3(e). In comparing the experimental $I(V)$ curves with the theoretical $R(E)$ spectra the experimental curves in these figures have been scaled in intensity and shifted in energy to match the energy location of high-energy peaks in the calculated spectra. This accounts for the theoretical uncertainty in the location of quasiparticle states (known as the band-gap problem), which is caused by our using an LDA-derived potential for the self-energy.[45] In the theoretical spectra, irrespective of the choice of V_i (the only adjustable parameter in the calculation), in coming from CeO_2 to Ce_2O_3 the characteristic conducting channel [$R(E)$ minimum] at $E - E_{VBM} = 11$ eV closes, and the reflectivity maximum moves to lower energies (peak B), so the maxima A and C turn into shoulders, see Fig. 2(b). On the contrary, the theoretical $R(E)$ curve for the hexagonal Ce_2O_3 [Fig. 4(d)] shows a dramatic difference to that of the cubic Ce_2O_3 and a striking disagreement with experiment. This rules out the formation of hexagonal Ce_2O_3 after cyclic reduction by methanol adsorption and subsequent thermal redesorption.

From a methodological perspective, the preceding discussion demonstrates that RPES and $I(V)$-LEEM should be viewed as complementary experimental techniques although both provide information on oxidation states: On one hand, RPES is highly sensitive to the presence of Ce^{3+} species and allows quantifying the cerium oxide stoichiometry of the near-surface region. On the other hand, $I(V)$-LEEM is highly sensitive to crystal structure while retaining sensitivity to stoichiometry changes within globally the same lattice. This latter aspect will be exploited when turning toward microscopic investigations targeting chemical reduction processes with lateral resolution, as presented in the following section.

D. Application to local surface reduction by methanol exposure

The theoretical analysis presented above correlates qualitative characteristics in the $I(V)$ curve shapes with certain electronic features in the material, which are related to its oxidation state. Furthermore, a comparison of the $I(V)$ curves for CeO_2 and cubic Ce_2O_3 suggests certain regions in electron kinetic energy in which the contrast in LEEM images can primarily be attributed to local differences in oxidation state. In the following demonstration, we have chosen a kinetic energy (15.4 eV) that is located near feature D of the $I(V)$ curve of CeO_2 [Fig. 2(b)] and where the trailing, "high-energy" slopes of the characteristic $R(E)$ peaks of reduced ceria are found. Hence, around this particular energy we expect an increased local reflectivity for a higher local oxidation state and a diminished local reflectivity for a lower local oxygen concentration. Also, our example will readily show that this energy is highly sensitive to changes in oxidation state [Fig. 5(d)].

In Fig. 5(a), a LEEM image of cerium oxide islands on Ru(0001) is displayed that has been recorded at an energy of 15.4 eV after growth at 800 °C and subsequent cool-down to RT. In the image, all ceria islands appear homogeneously bright, suggesting a uniform oxidation state after growth. However, significant intensity variations are observed after a single cycle of methanol adsorption, subsequent desorption of the reaction products by thermal annealing, and final cool-down to room temperature (RT) [Fig. 5(b)]. Therefore, this image contrast clearly indicates a local variation in oxidation

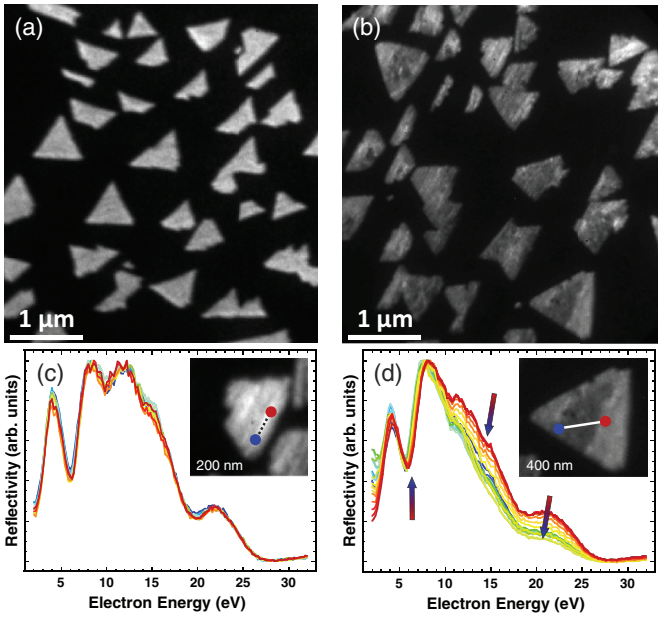

FIG. 5. (Color online) (a),(b) LEEM images ($E = 15.4$ eV) recorded (a) after growth and (b) after reduction by a single cycle of methanol exposure and subsequent annealing. The contrast on the ceria islands is due to local varying stoichiometry. (c),(d) Normalized local $I(V)$ curves acquired after reduction by methanol exposure [i.e., from image (b)] and extracted along indicated paths in 11-nm steps from single cerium oxide islands. In (c), the average oxidation state is almost constant while in (d) substantial variation is observed. The arrows in (d) indicate systematic changes in the $I(V)$ curves relating to local oxide reduction.

state. Interestingly, these brighter and darker patches show no apparent relation to the island shape or size.

While the preceding simplified analysis indicated differences in local oxidation state after reduction by methanol exposure, the amount of local reduction cannot readily be estimated from the intensity variation at a given energy. For a measure of the local oxidation state, the full set of local $I(V)$ curves needs to be investigated and compared to $R(E)$ reference spectra.

After reduction, local $I(V)$ curves [Figs. 5(c) and 5(d)] were extracted along selected paths in 11-nm steps (see insets). Only negligible intensity and shape variation are noticed when following a bright stripe [Fig. 5(c)], with the overall shape closely resembling the $CeO_2(111)$ reference spectra [Fig. 3(b)]. Therefore, we conclude that these stripes have not been reduced within the redox reaction and have remained fully oxidized ceria. Quite in contrast, the $I(V)$ curves extracted from areas of different brightness exhibit substantial, characteristic shape variations [Fig. 5(d)], namely the strong reduction in intensity near feature D, a concomitant significant decrease and left-shifting of feature E, and the gradual shifting of intensity from feature C, which appears to be composed of two separate peaks, toward B. Hence, we can deduce that the brighter and darker regions in Fig. 5(b) represent defective cerium oxide, i.e., $CeO_{2-\delta}(111)$, with few and many oxygen vacancies, respectively. Interestingly, the reduced cerium oxide regions do not seem to have formed predominantly at the oxide-metal phase boundary, as often assumed.

We note that the local $I(V)$ curves in Fig. 5(c) display an even closer match to the theoretical curve [Fig. 3(e)] than the experimental reference curve [Fig. 2(b)]. Since the main differences in sample preparation and $I(V)$ analysis are the significantly higher growth temperature, leading to the formation of well-defined ceria islands, and the lack of averaging in the subsequent nanoscale $I(V)$ curve extraction, we conclude that the apparent splitting of feature C, which is clearly predicted by theory, is directly related to the crystalline quality of cerium oxide.

IV. CONCLUSION

To summarize, using the surface chemistry of cerium oxide as an example, we have shown that the combination of low-energy electron microscopy and *ab initio* VLEED theory readily explains the LEEM image contrast observed in surface-chemical reduction-oxidation reactions, providing visual access to the local reduction of CeO_2 to Ce_2O_3 and hence the spatial distribution of oxygen vacancies. This approach has thus been shown to be a powerful tool for revealing local chemical transformations on the nanometer scale, and it has great potential for other correlated electron materials systems. By extending it to time-resolved measurements, novel insights into the dynamic behavior of inverse model catalyst systems under reaction conditions are expected.

ACKNOWLEDGMENTS

The authors would like to thank Percy Zahl, Peter Sutter (CFN, BNL), Gary Nintzel (NSLS, BNL), and Jürgen Lauckner (University of Bremen) for technical support as well as Verónica Ganduglia-Pirovano and Gustavo Murgida for helpful discussions. Research carried out in part at the Center for Functional Nanomaterials and the National Synchrotron Light Source, Brookhaven National Laboratory, which is supported by the US Department of Energy, Office of Basic Energy Sciences, under Contract No. DE-AC02-98CH10886. Partial support from the Spanish Ministerio de Ciencia e Innovación (Grant No. FIS2010-19609-C02-02) and the COST Action CM1104 is gratefully acknowledged.

*flege@ifp.uni-bremen.de

[1] A. Trovarelli (ed.), *Catalysis by Ceria Related Materials* (Imperial College Press, London, 2001).
[2] L. Vivier and D. Duprez, ChemSusChem **3**, 654 (2010).
[3] W. C. Chueh, C. Falter, M. Abbott, D. Scipio, P. Furler, S. M. Haile, and A. Steinfeld, Science **330**, 1797 (2010).
[4] C. Sun, H. Li, and L. Chen, Energy Environ. Sci. **5**, 8475 (2012).
[5] H.-J. Beie and A. Gnörich, Sens. Actuators B: Chem. **4**, 393 (1991).

[6]P. Jasinski, T. Suzuki, and H. U. Anderson, Sens. Actuators B: Chem. **95**, 73 (2003).
[7]D. Barreca, A. Gasparotto, C. Maccato, C. Maragno, E. Tondello, E. Comini, and G. Sberveglieri, Nanotechnology **18**, 125502 (2007).
[8]M. Fanciulli and G. Scarel (eds.), *Rare Earth Oxide Thin Films*, Topics in Applied Physics (Springer, Berlin, Heidelberg, 2007).
[9]H. C. Yao and Y. Y. Yao, J. Catal. **86**, 254 (1984).
[10]X. Courtois, N. Bion, P. Marécot, and D. Duprez, *Past and Present in DeNO$_x$ Catalysis* (Elsevier, Amsterdam, 2007).
[11]P. Arunkumar, M. Meena, and K. S. Babu, Nanomater. Energy **1**, 288 (2012).
[12]H. Kuhlenbeck, S. Shaikhutdinov, and H.-J. Freund, Chem. Rev. **113**, 3986 (2013).
[13]F. Esch, S. Fabris, L. Zhou, T. Montini, C. Africh, P. Fornasiero, G. Comelli, and R. Rosei, Science **309**, 752 (2005).
[14]S. Torbrügge, M. Reichling, A. Ishiyama, S. Morita, and O. Custance, Phys. Rev. Lett. **99**, 056101 (2007).
[15]A. Locatelli and E. Bauer, J. Phys.: Condens. Matter **20**, 093002 (2008).
[16]V. Heine, Proc. Phys. Soc. **81**, 300 (1963).
[17]G. Capart, Surf. Sci. **13**, 361 (1969).
[18]R. C. Jaklevic and L. C. Davis, Phys. Rev. B **26**, 5391 (1982).
[19]E. Bauer, *Physics of Solid Surfaces* (Elsevier, Amsterdam, 1988), pp. 26–36.
[20]V. N. Strocov, H. I. Starnberg, and P. O. Nilsson, Phys. Rev. B **56**, 1717 (1997).
[21]N. Barrett, E. E. Krasovskii, J.-M. Themlin, and V. N. Strocov, Phys. Rev. B **71**, 035427 (2005).
[22]E. E. Krasovskii and V. N. Strocov, J. Phys.: Condens. Matter **21**, 314009 (2009).
[23]W. Xu, R. Si, S. D. Senanayake, J. Llorca, H. Idriss, D. Stacchiola, J. C. Hanson, and J. A. Rodriguez, J. Catal. **291**, 117 (2012).
[24]J. I. Flege, E. Vescovo, G. Nintzel, L. H. Lewis, S. Hulbert, and P. Sutter, Nucl. Instrum. Methods Phys. Res., Sect. B. **261**, 855 (2007).
[25]P. Zahl, T. Wagner, R. Möller, and A. Klust, J. Vac. Sci. Technol. B **28**, C4E39 (2010).
[26]J. I. Flege, J. Hrbek, and P. Sutter, Phys. Rev. B **78**, 165407 (2008).
[27]B. Kaemena, S. D. Senanayake, A. Meyer, J. T. Sadowski, J. Falta, and J. I. Flege, J. Phys. Chem. C **117**, 221 (2013).
[28]W. F. Chung, Y. J. Feng, H. C. Poon, C. T. Chan, S. Y. Tong, and M. S. Altman, Phys. Rev. Lett. **90**, 216105 (2003).
[29]J. B. Hannon, J. Sun, K. Pohl, and G. L. Kellogg, Phys. Rev. Lett. **96**, 246103 (2006).
[30]J. I. Flege and P. Sutter, Phys. Rev. B **78**, 153402 (2008).
[31]D. R. Mullins, P. V. Radulovic, and S. H. Overbury, Surf. Sci. **429**, 186 (1999).
[32]V. Matolín, M. Cabala, V. Cháb, I. Matolínová, K. C. Prince, M. Škoda, F. Šutara, T. Skála, and K. Veltruska, Surf. Interface Anal. **40**, 225 (2008).
[33]V. Matolín, I. Matolínová, L. Sedláček, K. C. Prince, and T. Skála, Nanotechnology **20**, 215706 (2009).
[34]Relaxation of the outermost atomic layer was very recently found for CeO_2(111); see D. A. Siegel, W. C. Chueh, F. El Gabaly, K. F. McCarty, J. de la Figuera, and M. Blanco-Rey, J. Chem. Phys. **139**, 114703 (2013).
[35]J. I. Flege, A. Meyer, J. Falta, and E. E. Krasovskii, Phys. Rev. B **84**, 115441 (2011).
[36]Self-consistent calculations are performed with the full-potential linear augmented plane waves method as explained in E. E. Krasovskii, F. Starrost, and W. Schattke, Phys. Rev. B **59**, 10504 (1999).
[37]J. C. Slater, Phys. Rev. **51**, 840 (1937).
[38]E. E. Krasovskii, Phys. Rev. B **70**, 245322 (2004).
[39]H. C. Poon, S. Y. Tong, W. F. Chung, and M. S. Altman, Surf. Rev. Lett. **5**, 1143 (1998).
[40]V. N. Strocov, E. E. Krasovskii, W. Schattke, N. Barrett, H. Berger, D. Schrupp, and R. Claessen, Phys. Rev. B **74**, 195125 (2006).
[41]E. E. Krasovskii, K. Rossnagel, A. Fedorov, W. Schattke, and L. Kipp, Phys. Rev. Lett. **98**, 217604 (2007).
[42]E. E. Krasovskii, W. Schattke, P. Jiříček, M. Vondráček, O. V. Krasovska, V. N. Antonov, A. P. Shpak, and I. Bartoš, Phys. Rev. B **78**, 165406 (2008).
[43]E. E. Krasovskii, V. M. Silkin, V. U. Nazarov, P. M. Echenique, and E. V. Chulkov, Phys. Rev. B **82**, 125102 (2010).
[44]J. L. F. Da Silva, Phys. Rev. B **76**, 193108 (2007).
[45]H. Jiang, R. I. Gomez-Abal, P. Rinke, and M. Scheffler, Phys. Rev. Lett. **102**, 126403 (2009).
[46]V. I. Anisimov, J. Zaanen, and O. K. Andersen, Phys. Rev. B **44**, 943 (1991).
[47]V. I. Anisimov, I. V. Solovyev, M. A. Korotin, M. T. Czyżyk, and G. A. Sawatzky, Phys. Rev. B **48**, 16929 (1993).
[48]S. L. Dudarev, G. A. Botton, S. Y. Savrasov, C. J. Humphreys, and A. P. Sutton, Phys. Rev. B **57**, 1505 (1998).
[49]D. A. Andersson, S. I. Simak, B. Johansson, I. A. Abrikosov, and N. V. Skorodumova, Phys. Rev. B **75**, 035109 (2007).